



Fibrillarin is essential for S-phase progression and neuronal differentiation in zebrafish dorsal midbrain and retina

Stéphanie Bouffard^a, Emilie Dambroise^{a,1}, Alessandro Brombin^{a,2}, Sylvain Lempereur^{b,c}, Isabelle Hatin^d, Matthieu Simion^a, Raphaël Corre^{a,3}, Franck Bourrat^a, Jean-Stéphane Joly^{a,b}, Françoise Jamen^{a,*}

^a INRA CASBAH Group, Neurosciences Paris-Saclay Institute, CNRS, Université Paris-Saclay, Université Paris-Sud, Gif-sur-Yvette, France

^b Tefor Core Facility, TEFOR Infrastructure, NeuroPSI, CNRS, Gif-sur-Yvette, France

^c Université Paris-Est, LIGM, ESIEE, Noisy-le-Grand, France

^d Institut de Biologie Intégrative de la Cellule (I2BC), CEA, CNRS, Université Paris-Sud, Bâtiment 400, 91400 Orsay, France

ARTICLE INFO

Keywords:

Ribosome biogenesis
Danio rerio
 Cell cycle regulation
 Optic tectum
 Differentiation
 Neural progenitors

ABSTRACT

Fibrillarin (Fbl) is a highly conserved protein that plays an essential role in ribosome biogenesis and more particularly in the methylation of ribosomal RNAs and rDNA histones. In cellular models, FBL was shown to play an important role in tumorigenesis and stem cell differentiation. We used the zebrafish as an *in vivo* model to study Fbl function during embryonic development. We show here that the optic tectum and the eye are severely affected by Fbl depletion whereas ventral regions of the brain are less impacted. The morphogenesis defects are associated with impaired neural differentiation and massive apoptosis. Polysome gradient experiments show that *fbl* mutant larvae display defects in ribosome biogenesis and activity. Strikingly, flow cytometry analyses revealed different S-phase profiles between wild-type and mutant cells, suggesting a defect in S-phase progression.

1. Introduction

Fibrillarin (Fbl) is an essential nucleolar protein with a sequence and function conserved throughout evolution (Rodriguez-Corona et al., 2015; Shubina et al., 2016). This protein needs to associate with two other core proteins Nop56 and Nop58 and the RNA-binding protein 15.5-kDa in order to function as methyltransferase. Guided by C/D box small nucleolar RNAs (snoRNAs), fibrillarin catalyzes the 2'-O-methylation (2'-O-Me) of ribosomal RNAs (rRNAs). This post-transcriptional modification is crucial for the precise cleavage and maturation of rRNA, essential for its correct folding and association with ribosomal proteins (Mullineux and Lafontaine, 2012). The 2'-O-Me thus participates to the regulation of ribosome activity. Indeed it has been recently shown that the knockdown of FBL in human cells alters the intrinsic capacity of ribosomes to initiate translation from internal ribosome entry site (IRES) elements (Erales et al., 2017). Finally fibrillarin is also involved in the methylation of histone H2A at rDNA loci, and plays a major role in the regulation of rDNA transcription (Tessarz et al.,

2014).

Although ribosome biogenesis is a ubiquitous and fundamental process, fibrillarin expression level was recently shown to vary depending on physiological and pathological contexts (Marcel et al., 2013; Recher et al., 2013; Su et al., 2014; Watanabe-Susaki et al., 2014; Rodriguez-Corona et al., 2015). Previous functional studies on fibrillarin have highlighted its importance in several cellular process. In particular, loss-of-function analyses in yeast and mice have shown that fibrillarin is required for cell survival and early development (Schimmang et al., 1989; Newton et al., 2003). In addition, Watanabe-Susaki et al. showed in cell culture that FBL is important for cell homeostasis and stem cell identity, through the regulation of pluripotency and ability of pluripotent stem cells to differentiate (Watanabe-Susaki et al., 2014). FBL plays a particularly important role in cell cycle regulation, as highlighted by the abnormally high levels of this protein in several cancers, including human breast cancer (Marcel et al., 2013; Su et al., 2014), squamous cell cervical carcinoma (Choi et al., 2007) and prostatic intraepithelial neoplasia (Koh et al.,

* Corresponding author.

E-mail address: francoise.jamen@cnrs.fr (F. Jamen).

¹ Present address: INSERM U1163, Université Paris Descartes, Sorbonne Paris Cité, Institut Imagine, Paris, France.

² Present address: MRC Human Genetics Unit, MRC Institute of Genetics and Molecular Medicine, University of Edinburgh, Edinburgh, UK.

³ Present address: Institut Gustave Roussy, UMR8200, CNRS, Villejuif, France.

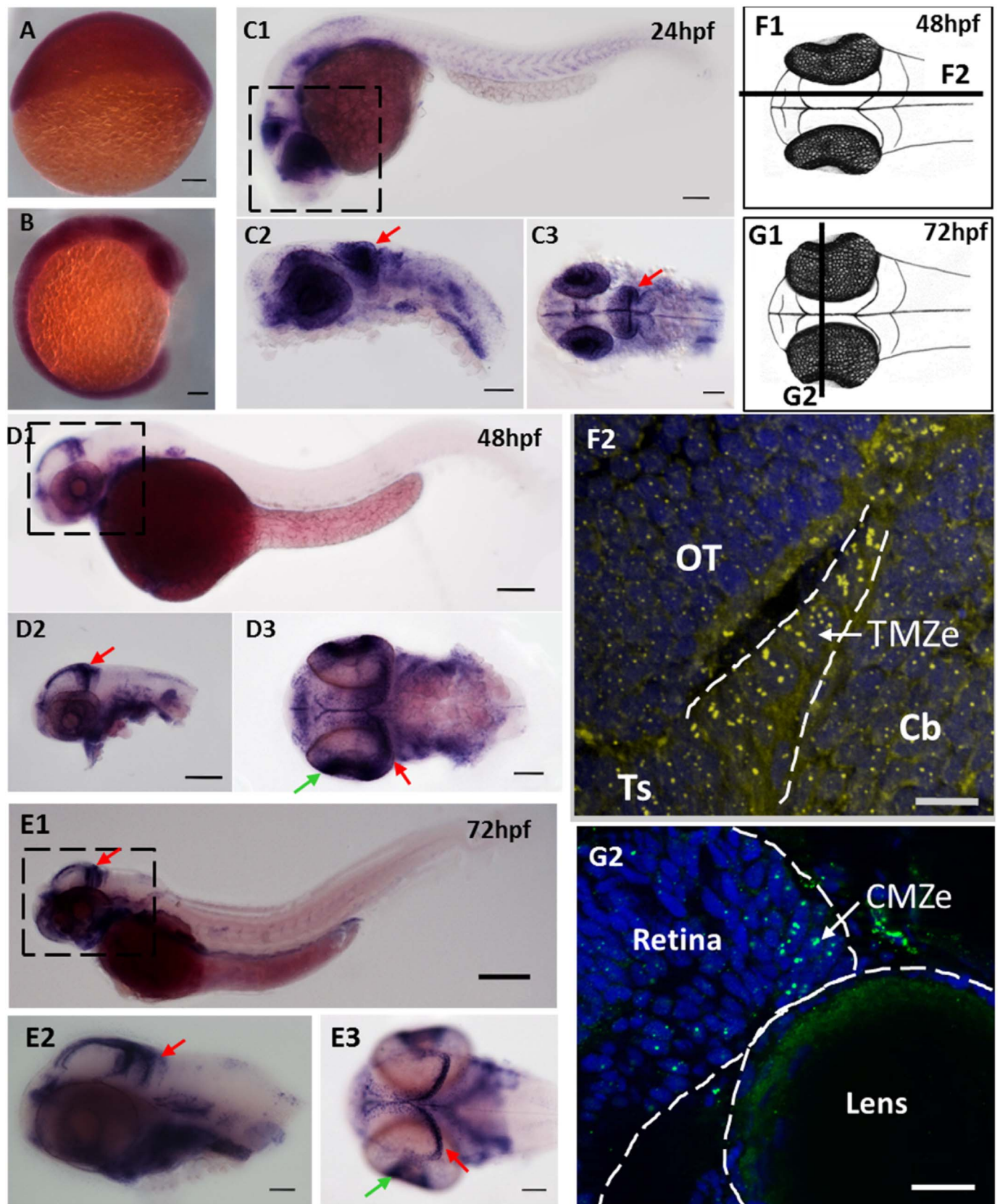


Fig. 1. *fbl* transcripts and Fbl protein are preferentially expressed in neural progenitors during zebrafish development. **(A–E)** *In situ* hybridization showing the progressive restriction of *fbl* expression during the development of zebrafish embryos **(A)** *fbl* is ubiquitously expressed at 6 hpf. **(B).** *fbl* expression begins to be restricted to highly proliferative regions (eyes, midbrain, and somites) during neurulation **(C)** At 24 hpf, *fbl* transcripts are abundant in the optic tectum (red arrows) and the retina. C1–C2: lateral views, C3: dorsal view **(D–E)** At 2 dpf **(D)** and 3 dpf **(E)**, *fbl* is preferentially expressed in the neuroepithelial progenitors of the TMZe at the periphery of the OT (red arrows), and in the external edge of the ciliary marginal zone (CMZe) of the retina (green arrows). Additional expression can be detected in the digestive system D1–D2 and E1–E2: lateral views, D3 and E3: dorsal views. Scale bars: 100 μ m. Anterior is to the left. **(F)** F1: Drawing of a 2dpf zebrafish embryo in dorsal view. The dark line corresponds to the sagittal section represented in F2. F2: Immunostaining showing Fbl protein on a sagittal section of a 2 dpf embryo. The Fbl protein, which is localized in the nucleoli, is present in all cells (yellow dots) but the punctate domains of expression are larger in TMZe neuroepithelial progenitors (surrounded by white dashed lines) than in other cells in the optic tectum (OT), cerebellum or *torus semicircularis*. **(G)** G1: Drawing of a 3dpf zebrafish embryo in dorsal view. The dark line corresponds to the transverse section represented in G2. G2: Immunostaining showing Fbl protein on a transverse section of a 3dpf embryo. The Fbl protein accumulates at the periphery of the retina where neuroepithelial cells are located (CMZe). Scale bars: 25 μ m. Ch: cerebellum; CMZe: external edge of the ciliary marginal zone; OT: optic tectum; Ts: *torus semicircularis*; TMZe: external edge of the tectal marginal zone.

2011). Marcel et al. also showed in breast cancer cell lines, that *FBL* overexpression leads to aberrant rRNA methylation, changes in ribosome activity, poor translation fidelity and an increase in the initiation of IRES-dependent translation for the products of cancer-related genes, such as IGF1R, c-Myc and FGF1/2 (Marcel et al., 2013). Conversely, the repression of *FBL* with siRNA decreases the proliferation of breast cancer cells (Su et al., 2014). Understanding the integrated roles of FBL in cell cycle regulation, cell proliferation and ribosome biogenesis has therefore become a real challenge.

The zebrafish is an ideal model for *in vivo* functional study. In zebrafish, the dorsal part of the midbrain, the optic tectum (OT) displays oriented growth during development, leading to the formation of ordered columns of cells with different levels of differentiation, from the periphery towards the center of the structure (Nguyen et al., 1999; Deves and Bourrat, 2012). This cellular model is thus ideal for studies of the specific role of Fbl in cell cycle regulation and cell homeostasis (Joly et al., 2016). At early stages of development, the proliferative neural population is located throughout the alar plate. Following somitogenesis, progenitor cells differentiate into functional neurons, which are found at the center of the OT. However, proliferation persists in a small zone of the midbrain, at the periphery of the optic tectum. This zone, homologous to the proliferative zone of the retina, is called the tectal marginal zone (TMZ; Joly et al., 2016).

Using live imaging, we previously identified two types of progenitors on the basis of their rates of proliferation in the transparent embryo (Recher et al., 2013). The neuroepithelial progenitors located at the external edge of the TMZ (TMZe) are slow-amplifying progenitors (SAPs). SAPs divide and give rise to fast-amplifying progenitors (FAPs) located in the intermediate layer (TMZi, (Joly et al., 2016). Each cell population is characterized by the preferential expression of various genes. In particular, transcripts encoding ribosome biogenesis factors, such as components of the box C/D complex, and Fbl in particular, are strongly expressed in SAPs, whereas these “house-keeping” genes are less strongly expressed in FAPs and differentiated cells (Recher et al., 2013). These striking observations led us to suggest that Fbl might be involved in cell cycle regulation in the slow-amplifying progenitors. We therefore performed an *in vivo* functional analysis of Fbl by characterizing zebrafish mutants for *fbl*. Homozygous mutant embryos showed strong defects in the brain and eyes development. Indeed, we observed a decrease in the volume of the central nervous system with increased apoptosis and deregulation of the cell cycle observed in the head. In addition, mutant larvae displayed specific defaults of neuronal differentiation in the visual system. Our findings highlight, for the first time *in vivo*, the importance of Fbl in midbrain development and the regulation of S-phase progression.

2. Results

2.1. Neuroepithelial slow-amplifying progenitors (SAPs) express high levels of fibrillarin transcripts and proteins

We first characterized the *fibrillarin* (*fbl*) gene expression pattern during zebrafish embryogenesis, by whole-mount *in situ* hybridization (WMISH). We found that *fbl* was ubiquitously expressed during gastrulation (6 h post-fertilization (hpf), Fig. 1A). At the onset of

neurulation, Fbl mRNAs begins to accumulate in the eyes, brain and somites (Fig. 1B). From 1 day post-fertilization (dpf), *fbl* expression begins to be restricted to the OT, retina, gut and somites (Fig. 1C2–C3). At the long-pec (2 dpf) and protruding mouth (3 dpf) stages, high levels of *fbl* expression are observed at the periphery of the OT, in the external tectal marginal zone (TMZe) in which SAPs divide (Fig. 1D1–D3, E1–E3). These results demonstrated that *fbl* expression is thus progressively restricted during zebrafish embryogenesis. Immunohistochemistry (IHC) analysis revealed the presence of Fbl protein in all tectal cells, within the nucleoli, but this protein was more abundant at the extreme edge of the OT, where the SAPs are found (Fig. 1F1–F2). Fbl protein is also expressed at the extreme edge of the retina, in the ciliary marginal zone (CMZ), in which the progenitors and stem cells are localized (Fig. 1G1–G2). Thus Fbl is preferentially expressed in the proliferating cells of the OT and retina, which are thought to be sister cell types (Joly et al., 2016). These findings strongly suggest that Fbl may play an essential role in tectal and retinal cell proliferation.

2.2. Mutation of the zebrafish *fbl* gene leads to a smaller brain volume and larval death

We investigated the function of Fbl in tectal cell proliferation, in a *fbl*^{hi2581Tg} mutant zebrafish line that was previously generated by inserting a 6 kb retroviral sequence into the 5'UTR of the *fbl* gene (Amsterdam et al., 2004). By RT-qPCR, no *fbl* mRNA has been detected in mutant embryos from 24hpf, confirming that *fbl*^{hi2581Tg} is a null mutant (Fig. 2A).

Heterozygous embryos developed normally. By contrast, homozygous *fbl*^{hi2581Tg} mutant embryos began to display phenotypic differences relative to their control siblings as early as 24 hpf (Fig. 2B). From this stage onwards, tissue disorganization was observed, particularly in the head (Fig. 2B2, black arrow). At 2 dpf (Fig. 2B3–B4) and 3dpf (data not shown), homozygous mutants exhibited abnormal pigmentation, smaller eyes and heads, pericardiac edema, and a larger and rounder yolk with a thinner yolk extension than the wild type. At 4 dpf, the brain abnormalities became more pronounced, probably due to general defects along the whole body axis of the embryo (data not shown). The *fbl*^{hi2581Tg} larvae had a smaller body, with an increasingly curved tail, and they died by day 4 or 5 post-fertilization.

To determine whether the observed defects in mutant embryos were due to the loss of Fbl, rescue experiments were carried out by injecting mRNA encoding wild-type Fbl. Injection of 200 pg of *fbl* mRNA induced severe developmental defects (cyclopia, absence of head, truncated body) and high level of mortality (data not shown). We thus decreased the injection dose to 100 pg. At this dose, only 1.6% of the injected embryos at 48 hpf displayed a mutant phenotype while 24.7% were observed in non-injected embryos, percentage expected for homozygous mutants following a *fbl*^{hi2581Tg} heterozygote incross. Most importantly, 17.3% of the injected embryos displayed a rescued phenotype although slightly smaller eyes than in wild-type embryos were still observed (Fig. 2B5–B6, C). Thus taken together these results show that *fbl* mRNA largely rescued the mutant phenotype and that the defects observed in *fbl* mutants result from the loss of Fbl.

We quantified brain defects at 3 dpf, by measuring the volume of

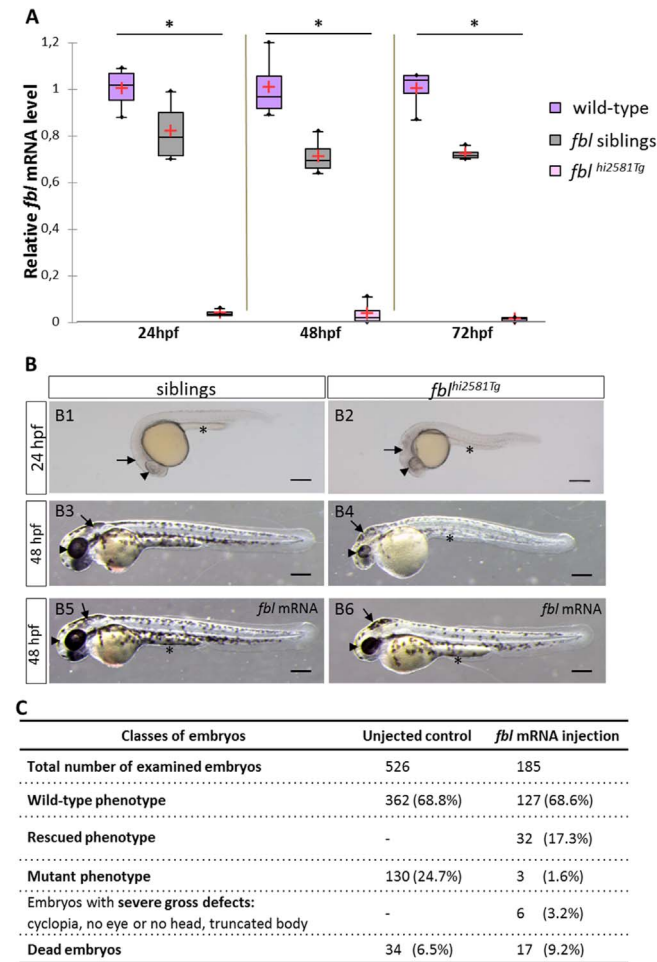


Fig. 2. Gross morphological defects in *fbl* null mutants are mainly seen in the head and eyes and are rescued by injection of *fbl* mRNA. **(A)** RT-qPCR quantification of relative levels of *fbl* mRNA at the indicated developmental stages shows the absence of *fbl* expression in mutants as early as the 24 hpf stage. Purple: wild-type, gray: siblings, pink: mutants. Statistical analyses were performed on four biological samples per condition. p-value (Kruskal-Wallis test) polysomes: 0.02. n.s., non-significant. **(B1-B6)** Lateral views of live embryos with anterior to the left and dorsal up. **(B1-B2)** *fbl*^{hi2581Tg} mutants start to display phenotypic abnormalities as early as the 24 hpf stage with necrosis in the midbrain area, slightly smaller eyes and a thin yolk extension. **(B3-B4)** At 48 hpf, mutant embryos have smaller eyes and smaller head than their siblings. In addition, mutant embryos display less pigmentation, pericardiac edema, a larger and rounder yolk and a thinner yolk extension. **(B5-B6)** At 48 hpf, *fbl* mutant embryos are largely rescued by *fbl* mRNA. In injected mutants, midbrain and yolk extension look similar in size to the ones in siblings. The size of the eye is bigger than in not injected mutants although remaining slightly smaller than in siblings. In panels B1-B9, eyes, midbrain area and yolk extension are respectively indicated by arrowheads, arrows and asterisks. Scale bar = 200 μ m. **(C)** Classes of phenotypes of *fbl* mRNA injected embryos from an *fbl*^{hi2581Tg} incross. A strong decrease in the number of injected embryos with mutant phenotype is observed indicating that the *fbl* mRNA rescues the mutation.

the central nervous system (CNS; including brain and eyes): we stained lipidic structures with DiI, obtained 3D images by confocal microscopy and manually segmented the brain (Fig. 3A).

CNS volume was significantly smaller in *fbl*^{hi2581Tg} larvae than in their wild-type or heterozygous at the same developmental stage. More precisely, CNS volume in the mutants was one third smaller than in their siblings or the wild-type larvae (Fig. 3B). We also quantified the eye volume in *fbl* mutant, siblings and wild-type larvae. Interestingly, the eye volume of the mutant larvae was five times reduced in comparison with the siblings and wild-type larvae (Fig. 3C). Taken together, these data suggest a role of Fbl in the development of the brain and the eye.

2.3. Ribosome biogenesis is affected in *fbl*^{hi2581Tg} mutant embryos

Fbl is involved in the methylation of rRNA and rDNA histones. We therefore hypothesized that *fbl* loss of function would lead to lower levels of rDNA transcription and a disruption of ribosome biogenesis. Ribosome biogenesis begins with the transcription of the 47S intermediate rRNA, which contains a 5' externally transcribed sequence (ETS) and two internally transcribed sequences (ITS1 and ITS2). The intermediate 47S rRNA is processed after its transcription: the 5' ETS is cleaved first, followed by the ITS1 and ITS2, to generate the mature 18S, 5.8S and 28S rRNAs. The 5' ETS, ITS1 and ITS2 are used to estimate relative rRNA transcription levels.

We used RT-qPCR to investigate rDNA transcription and rRNA processing by quantifying the levels of 5'ETS, 18S, ITS1 and ITS2 rRNA. At 3 dpf, 18S mature rRNA levels were significantly lower (of 93%) in *fbl*^{hi2581} larvae, whereas we did not observe any significant differences in *fbl* siblings larvae and wild-type larvae (Fig. 4A). Surprisingly, 5' ETS rRNA levels were slightly higher in *fbl*^{hi2581Tg} larvae than in the wild type. However, ITS1 and ITS2 rRNA levels did not differ between the three genotypes (Fig. 4A). Overall, these data indicate that 47S rDNA transcription is not impaired in *fbl*^{hi2581} mutant embryos, but that rRNA processing is greatly impaired, as demonstrated by the relative levels of mature 18S rRNA.

As 18S rRNA processing is considered to be a rate-limiting step in ribosome biogenesis (Laferte et al., 2006), we hypothesized that impaired rRNA processing in *fbl*^{hi2581Tg} mutant embryos and possible subsequent alterations to rRNA posttranslational modifications would result in an overall decrease in ribosome biogenesis. We used polysome profiling to evaluate ribosome biogenesis in 3 dpf *fbl* mutant embryos, control siblings and wild-type embryos (Fig. 4B-C). Fewer polysomes were observed in the mutants as compared to the wild-type larvae. The polysomal fraction, which corresponds to ribosomes bound to mRNA, provides an indication of the translational activity of the ribosomes. Polysome peaks were smaller for the mutant larvae than for their siblings and wild-type larvae, indicating that smaller numbers of ribosomes were bound to mRNA in the mutants (Fig. 4B). Thus, for every seven ribosomes binding mRNA in wild-type and sibling embryos, only five were bound to mRNA in *fbl*^{hi2581} embryos. We measured the area under each peak, and calculated the ratio between the 80S and polysome peaks (Fig. 4B-C). The polysome ratio was lower in the mutants than in the wild-type embryos, highlighting lower levels of ribosomal activity.

We performed similar experiments at 2 dpf, when the embryos are less affected. Despite the similarity of the defects observed (data not shown), differences in ribosome biogenesis between wild-type and mutant embryos were less marked. This is not surprising and highlights the worsening of the phenotype as development proceeds. Collectively, these data suggest that *fbl* mutation leads to an impaired ribosome biogenesis at late steps of the pathway and lower levels of ribosome activity.

2.4. The dorsal midbrain and the retina are the most strongly affected structures in the *fbl*^{hi2581Tg} brain

We demonstrated that *fbl*^{hi2581Tg} larvae display smaller CNS. To further characterize those brain defects, we analyzed different regions of the brain by DiI and Elavl3 (marker of neural differentiation) labeling and generated 3D visualization of the stained larvae (supplemental data, movie 1). Several basal domains, such as the ventral telencephalon, olfactory epithelium and hypothalamus, were recognizable but disorganized (Fig. 5A). We also detected the presence of the tracts of the anterior (tac) and post-optic commissures (tpoc), as well as the optic recess region (ORR, Affaticati et al., 2015) which are ventral/basal brain structures (Fig. 5A). Overall, these data suggest that the *fbl* mutation leads to more or less correct differentiation events in the ventral part of the brain, and to the generation of most of the domains of the brain.

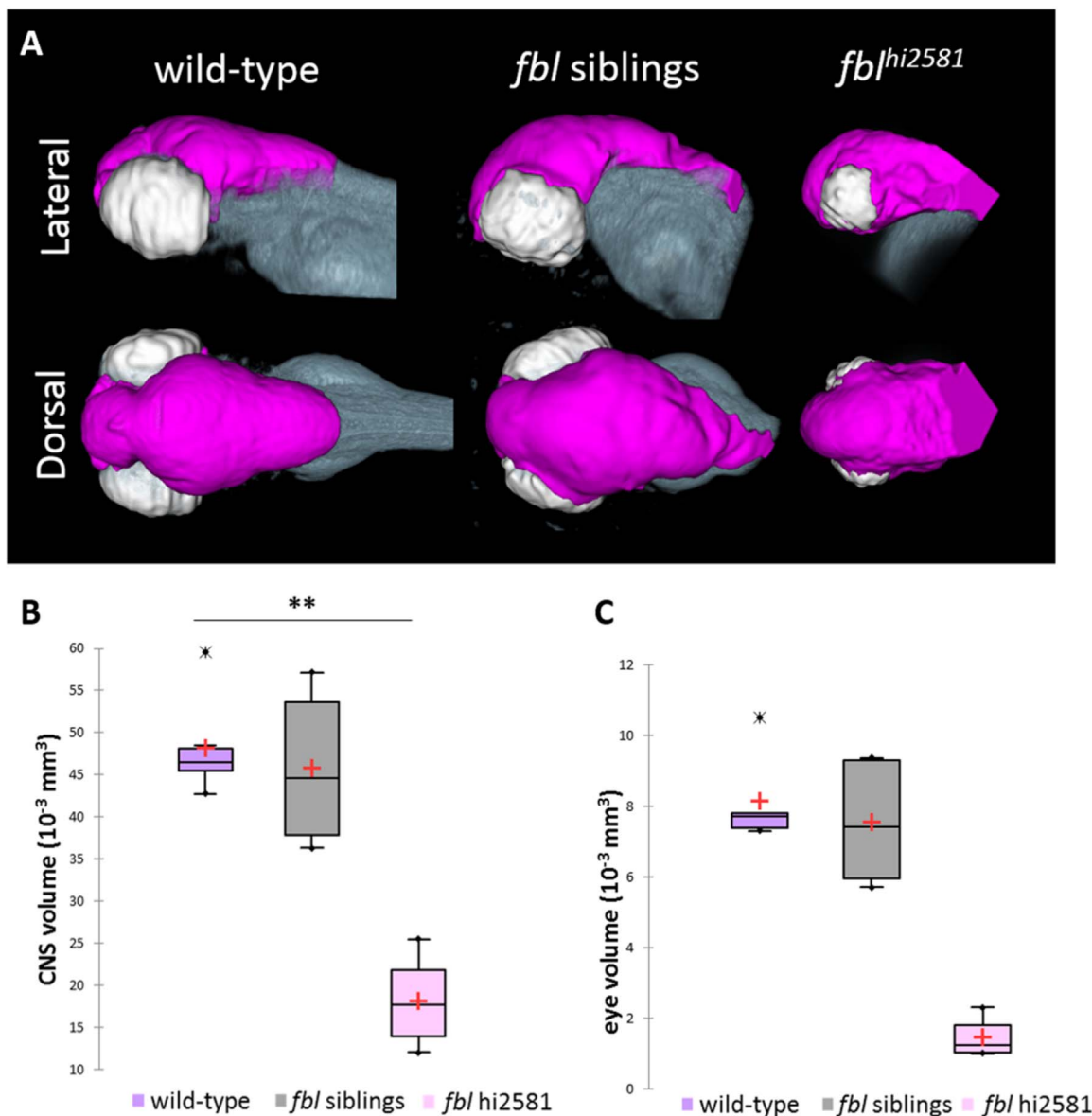


Fig. 3. The *fbl*^{hi2581Tg} mutation mostly affects midbrain structures from 24 hpf. **(A)** Volume rendering of the DiI-positive domains (gray) and surface rendering of a manual segmentation of the CNS (magenta) and eye (white) based on the DiI signal in 3dpf wild-type, *fbl* siblings and *fbl*^{hi2581Tg} mutant embryos. *fbl* mutant larvae display an apparent reduction of the CNS volume compared to their siblings or wild-type larvae. Lateral views: anterior to the left, dorsal to the top. Dorsal view: anterior to the left, right to the top. **(B)** Quantification of mean CNS volume highlights a significant difference between *fbl* mutants, their siblings and wild-type larvae. Statistical analyses were performed on six samples per condition. *p*-value: .003 (Kruskal-Wallis test). **(C)** Quantification of mean eye volume highlights a significant difference between *fbl* mutants, their siblings and wild-type larvae. Statistical analyses were performed on the mean size of both eye of six samples per condition. *p*-value: .005 (Kruskal-Wallis test). Purple: wild-type, gray: *fbl* siblings, pink: *fbl*^{hi2581Tg}. Scale bar: 100 μ m. Anterior is to the left.

Supplementary material related to this article can be found online at <http://dx.doi.org/10.1016/j.ydbio.2018.02.006>.

At 3dpf, the wild-type retina is organized as a cortical structure with distinct layers: layers of neurons labeled with Elavl3 and plexiform layers (Fig. 5A1). In mutant embryos, we see a nearly complete absence of Elavl3 labeling, indicating that in the retina, there is no neuronal differentiation (Fig. 5A2).

Surprisingly, histological analyses revealed that 2 dpf mutants had a smaller tectum than their siblings (Fig. 5B). Moreover, acellular zones were detected in this midbrain structure (Fig. 5B2–B4). However, the proliferative region of the TMZe seemed to be correctly formed, but thicker than stage-matched WT embryos (Fig. 5B2, white arrows). Thus, the mutation strongly affects the dorsal midbrain and retina, structures in which the *fbl* gene is preferentially expressed, consistent with a specific role for Fbl in these regions.

Fbl is known to be required for the maintenance of normal nucleolar morphology (Amin et al., 2007; Ma et al., 2016). We therefore studied nuclear and nucleolar morphologies in control and mutant embryo midbrains. DAPI staining of the nucleus revealed differences in nuclear shape between *fbl* mutant larvae and their siblings (Fig. 5C, purple). Wild-type embryos had round nuclei at the center of the OT and in FAPs. By contrast the nuclei in the SAPs were more elongated and had larger nucleoli (Recher et al., 2013). Surprisingly, in *fbl*^{hi2581Tg} embryos, the nuclei of cells over the entire surface of the tectum were elongated, and resembled those of wild-type SAPs (Fig. 5C).

By contrast, the nuclei of the ventral structure of the midbrain, the torus semicircularis (TS) presented no change in shape (data not shown). On 3D views, we selected the larger axis of the nuclei for measurements. The quantification of nuclear diameters in the OT and

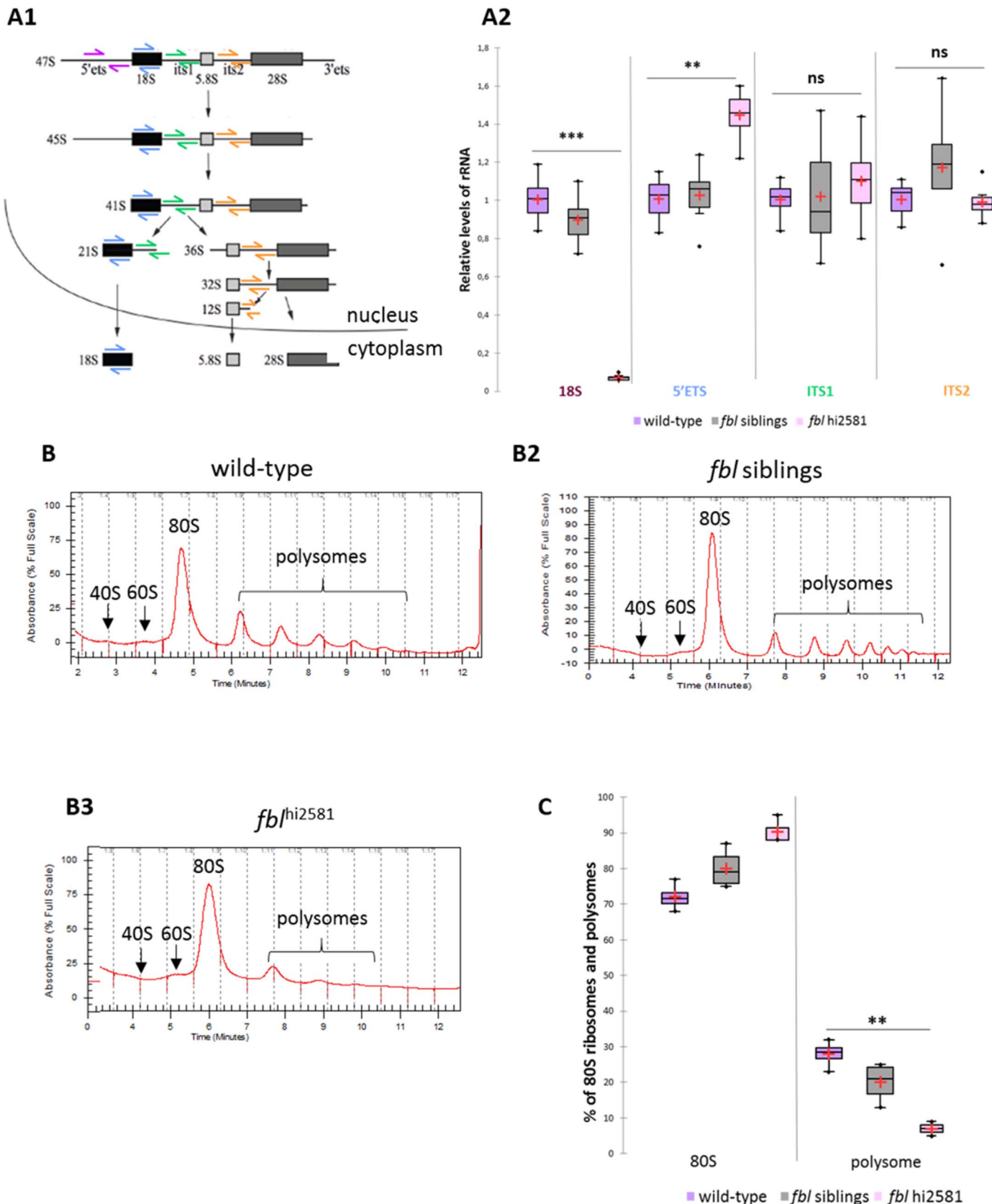


Fig. 4. Ribosome biogenesis is impaired in *fbl* mutant embryos. **(A)** RT-qPCR quantification of 5'ETS, ITS1, ITS2 and 18S rRNAs in mutant, siblings and wild-type larvae at 3 dpf. **A1:** Scheme of rRNA processing, adapted from (Le Bouteiller et al., 2013). Arrows indicate the location of the amplified regions: 18S: purple, 5'ETS: blue, ITS1: green and ITS2: orange. **A2.** Mutant embryos have lower levels of 18S rRNA (93% lower). **(B)** Polysome profiling of 3 dpf wild-type (**B1**), *fbl* siblings (**B2**) and *fbl*^{hi2581Tg} mutant (**B3**) embryos showed a lower polysome ratio in *fbl*^{hi2581Tg} larvae, indicating impaired ribosomal activity in these larvae. **(C)** Quantification of the relative proportions of 80S and polysomes (ratio of the 80S or polysome area with global area). Statistical analyses were performed on four samples per condition. *p*-value (Kruskal-Wallis test) polysomes: 0.0041. Purple: wild-type, gray: *fbl* siblings, pink: *fbl*^{hi2581Tg}.

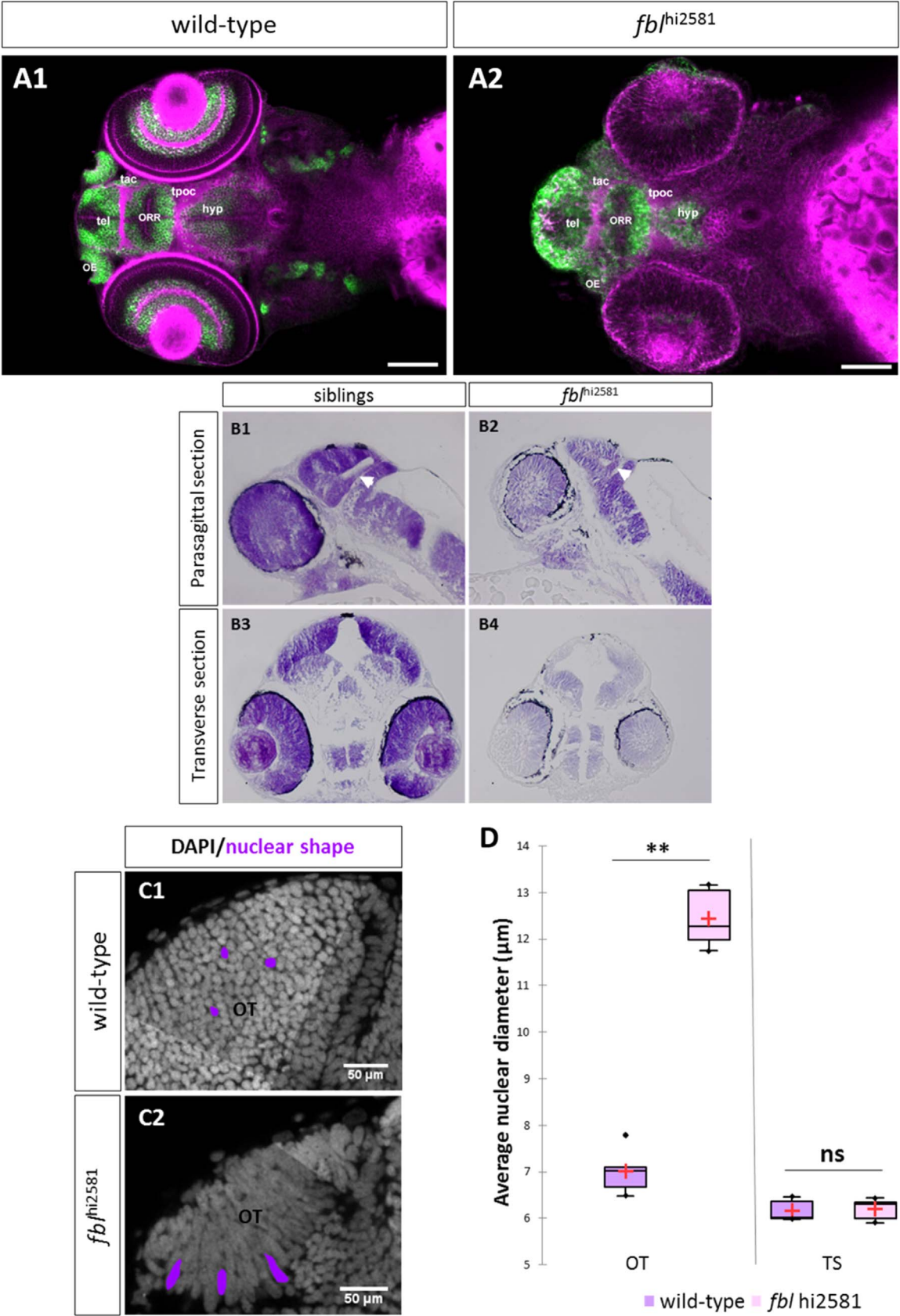


Fig. 5. *fbl* mutants have specific midbrain and retina defects. **(A)** Horizontal optical sections of Elavl3 (marker of neural differentiation) immunolabelling and DiI staining in wild-type **(A1)** and mutant **(A2)** embryos at 3dpf. Pink: DiI labeling, Green: Elavl3 staining. Scale bars: 100 μ m. Anterior is to the left. Most brain domains and axon tracts are present but have a disrupted organization in *fbl* mutant embryos. **(B)** Sagittal (A1–A2) and transverse (A3–A4) paraffin sections of wild-type (left) and *fbl*^{hi2581Tg} mutant (right) embryos at 2dpf. Histological analysis with cresyl violet staining revealed smaller tecta and acellular zones in the mutant embryos. The proliferation region (TMZe) is thicker in the mutant embryos (white arrow) **(B2, B4)** than in their siblings **(B1, B3)**. Anterior is to the left. **(C)** Nuclear labeling (DAPI) in the optic tectum of 2dpf wild-type **(C1)** and mutant **(C2)** embryos at 2dpf, showing the larger nuclear diameter in the tectum of mutant larvae. Scale bar: 50 μ m **(D)** Quantification of the nuclear diameter of wild-type (purple) and *fbl*^{hi2581Tg} (pink) 2dpf embryos. Nuclear diameters were measured with Fiji software. We measured the longest dimension of 50 nuclei on selected 2D images of the nuclei of 2 dpf embryos. Statistical analyses were performed on the mean diameters of nuclei from five mutant or wild-type embryos. *p*-value (Mann & Whitney test) OT: 0.008; *p*-value TS: 1.000. Hyp: hypothalamus, OE: olfactory epithelium, ORR: optic recess region OT: optic tectum, tac: tract of the anterior commissure, tel: telencephalon, tpoc: tract of the post-optic commissure, TS: *torus semicircularis*.

TS of wild-type and mutant embryos indicated a specific increase of the area within the OT, with no change in the TS (Fig. 5D). Indeed, wild-type tectal nuclei had a mean longest diameter of 7 μ m, whereas *fbl*^{hi2581Tg} tectal nuclei reached diameters of up to 12 μ m. By contrast, the nuclei in the TS of both mutant and wild-type embryos had a mean diameter of 6 μ m. These findings suggest that the dorsal part of the midbrain was most affected in *fbl* mutant embryos.

2.5. Neuronal specification and differentiation are impaired in mutant embryos

The observed dorsal midbrain patterning defects suggested that neural specification and differentiation might also be impaired in this region. We first addressed this question by quantifying *neuroD1* mRNA levels by RT-qPCR to assess neural specification. Interestingly, we found that *neuroD1* expression levels were 91% lower in mutant embryos than in wild-type embryos (Fig. 6A). Neural specification was, therefore, disrupted in *fbl* mutant embryos.

We also analyzed neural tissue specification in different regions of the brain, by analyzing by *in situ* hybridization (ISH) the expression pattern of *eomes* and *otx2*, which are involved in the specification of the anterior territories of the developing brain. *Otx2* expression is an anterior brain marker in the neural tube but becomes restricted to the developing midbrain later in development, whereas *eomes* is specifically expressed in the forebrain. In mutant embryos, at both 2 dpf (Fig. 6B1–B2) and 3 dpf (data not shown), *eomes* expression was maintained in the developing forebrain. By contrast, *otx2* expression was affected in the dorsal midbrain of mutants, whereas the expression of this gene was unaffected in the most ventral and anterior domains in mutants (Fig. 6B3–B4). These findings confirm the presence of mid-brain-specific defects in neural specification in *fbl* mutant embryos.

We then analyzed neural differentiation by immunohistochemical staining for Elavl3, a marker of neural differentiation. Neural differentiation begins at 2 dpf in wild-type embryos, and tectal Elavl3-positive neurons are located in the center of the optic tectum. At this stage, no Elavl3 labeling was detected in mutant embryos (Fig. 6C).

We investigated possible links between this phenotype and developmental delay, by analyzing neural differentiation at 3 dpf. In *fbl*^{hi2581Tg} embryos, no Elavl3-positive neurons were detected in the dorsal midbrain at 3 dpf (Fig. 6D–E), whereas a few Elavl3-positive neurons were detected ventrally in the TS (Fig. 6E) and posteriorly in the spinal cord (data not shown). These data indicate that neural differentiation is specifically impaired in the dorsal midbrain structures of *fbl*^{hi2581Tg} mutant embryos.

These results suggest that the neuronal lineage is specifically disrupted in the dorsal midbrain of *fbl* mutants. This finding is consistent with a tissue-specific role of *Fbl* in midbrain morphogenesis.

2.6. Mutant cells undergo massive apoptosis

We investigated the mechanisms underlying the apparent decrease in tectum neuronal differentiation and the presence of acellular zones in the OT, by evaluating the role of *fbl* in cell survival. We therefore performed TUNEL staining (Fig. 7), to label DNA breaks. At 24 hpf, cell death rates were higher in *fbl*^{hi2581Tg} mutant embryos than in wild-type embryos (Fig. 7A). Cell culture studies have shown that the knockdown

of *FBL* expression induces p53 activation (Su et al., 2014). We therefore hypothesized that the apoptosis observed in *fbl* mutant embryos might be p53-mediated. Quantitative RT-PCR revealed that *tp53* transcript levels were significantly higher in mutant embryos than in wild-type embryos at 24 hpf, 48 hpf and 72 hpf (Fig. 7B–C). These results suggest that the atrophy of the optic tectum in *fbl*^{hi2581Tg} mutant embryos may result from *tp53*-dependent apoptosis.

2.7. The spatial distribution of proliferative cells is disorganized in *fbl* mutant embryos

Hypoplasia may result from an increase in apoptosis and/or an inhibition of proliferation. In 2 dpf wild-type embryos, proliferation is restricted to the periphery of the OT. We analyzed the total proliferating cell population by immunostaining for PCNA (proliferating cell nuclear antigen). Strikingly, at 2 dpf (Fig. 8A) and 3 dpf (data not shown), PCNA labeling was observed in most of the tectal cells of the mutant larvae (Fig. 8A1), whereas it was spatially restricted to a subset of tectal cells present at the periphery in the wild type larvae (Fig. 8A2). These findings suggest that all the cells of the OT are proliferating in mutant embryos.

We then analyzed DNA replication by monitoring the incorporation of a thymidine analog (EdU). After a two-hour pulse, we were able to determine the location of the actively dividing cells. In WT embryos, at 2 dpf, EdU incorporation was observed at the OT margins and in the TMZe. By contrast, EdU-positive cells were found scattered over the entire optic tectum in mutant embryos (Fig. 8B2). We observed the same unrestricted pattern of EdU incorporation at a later stage (3 dpf, data not shown). However, the quantification of EdU-positive cells over the entire OT showed that about 40–50% of tectal cells were positive for EdU in both mutant and wild-type embryos (Fig. 8C).

Similarly, pH3 (phospho-histone 3) staining, which labels cells in M-phase showed that mitotic cells were not restricted to the margin in mutant embryos (Fig. 8D). Quantification of the population of mitotic cells within the OT revealed no difference in the proportion of this population between mutant and wild-type embryos at 2 dpf (Fig. 8E).

Taken together, these data reveal the presence of a cell-cycle defect, with a larger population of proliferative cells and an abnormal distribution of actively dividing cells in the tectum of mutant embryos.

2.8. S-phase progression is impaired in *fbl* mutant embryos

We assessed the cell cycle profiles of mutant cells more precisely and determined whether the rate of cell cycling differed between wild-type and mutant embryos, by analyzing DNA content by Fluorescence-Activated Cell Sorting (FACS). For this purpose, we incorporated EdU for 2 h at 3dpf, in both mutant and wild-type embryos, and then labeled the DNA with the intercalating agent 7-AAD (7-aminoactinomycin D). We carried out FACS analyses on dissociated cells from the dissected heads of control and mutant embryos. In wild-type embryos (Fig. 9A), 80% of the cells, on average, were in G0/G1 phase. Less than 1% of the cells were in G2/M phase and 7–8% were in S-phase. An additional phase, the SubG1, consisting of cell aggregates and dying cells, accounted for 5% of all cells in the heads. The distribution of cells in the different phases of the cell cycle in *fbl* mutant embryos (Fig. 9B) was similar to that in wild-type embryos (Fig. 9C).

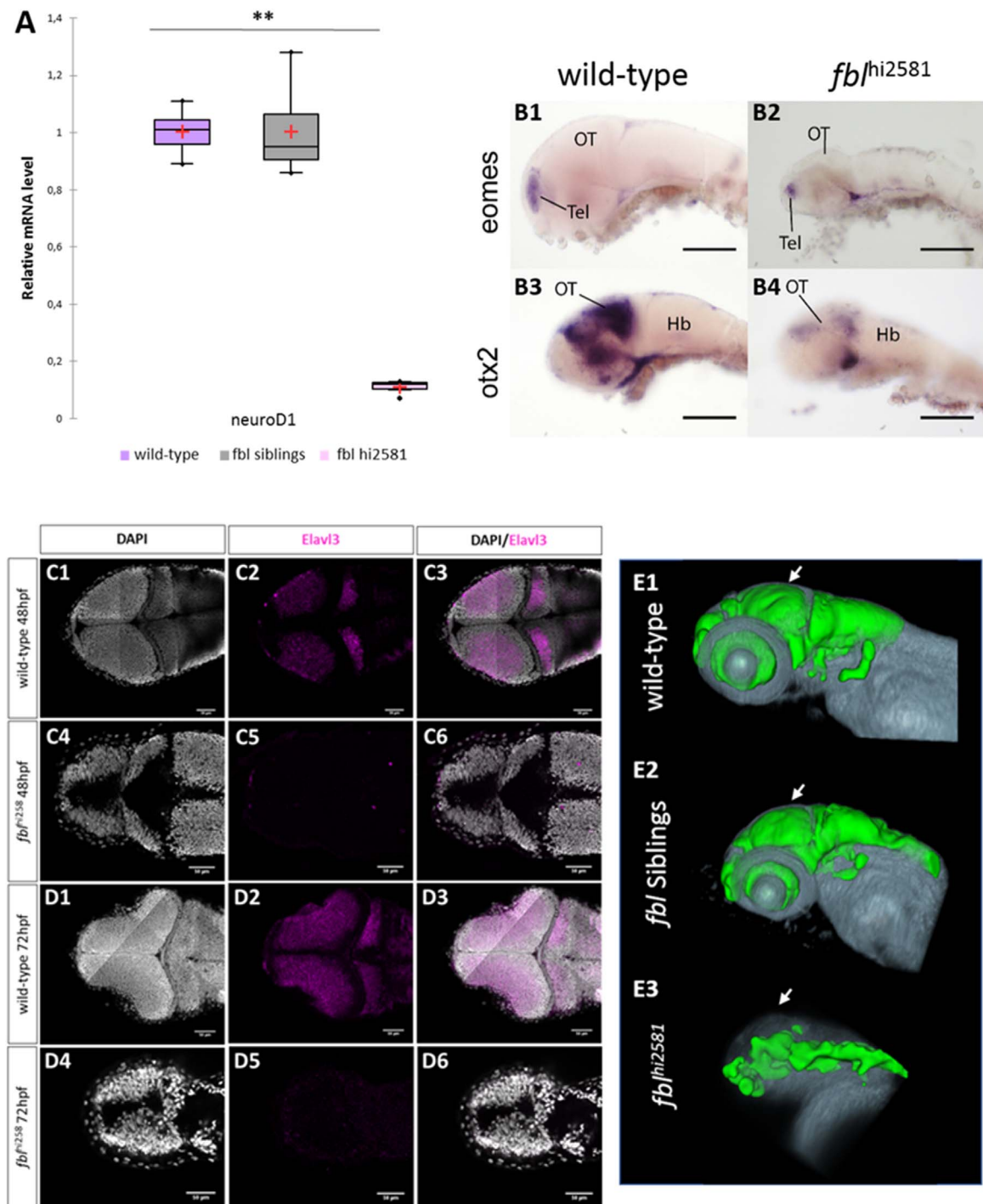


Fig. 6. Neural specification and neural differentiation are impaired in *fbl*^{hi2581Tg} mutant embryos. **(A)** RT-qPCR quantification of the relative levels of *neuroD1* mRNA. Purple: wild-type, gray: siblings, pink: mutants. **(B)** Expression patterns of *eomes* (B1–B2), a marker of forebrain specification, was similar in wild-type and mutant embryos, whereas that of *otx2* (B3–B4), a marker of midbrain specification, is absent in *fbl*^{hi2581Tg} mutant embryos. Scale bars: 50 μm. Hb: hindbrain, OT: optic tectum, Tel: telencephalon. **(C)** Horizontal optical sections of *elavl3* (marker of neural differentiation) labeling in 2 dpf wild-type (C1–C3) and mutant (C4–C6) embryos and in 3 dpf wild-type (D1–D3) and mutant (D4–D6) embryos. Gray: DAPI staining, pink: Elavl3 staining. Scale bars: 50 μm. Anterior is to the left. **(E)** Volume rendering of the DiI-positive domains (gray) and surface rendering of a manual segmentation of the Elavl3-positive (green) domains in 3 dpf wild-type (E1), *fbl* siblings (E2) and *fbl*^{hi2581} mutant embryos (E3). For lateral views, anterior to the left and dorsal to the top. White arrows point out to the midbrain. Neural differentiation is specifically impaired dorsally in *fbl* mutant.

We concluded that mutant cells were not blocked in any phase of the cell cycle and seemed to cycle in a similar manner to wild-type embryo cells.

However, 7-AAD/EdU flow cytometry revealed a marked difference in S-phase profiles on histogram plots (Fig. 9B), with lower levels of EdU incorporation for cells in *fbl* mutants than in wild-type larvae.

This indicates that either mutant cells incorporate EdU less efficiently than wild-type cells, or that they die in S-phase. We quantified these differences in profile, by analyzing the distribution of cells within S-phase through determinations of the percentages of cells in early S, mid-S and late S phase (Fig. 9D). In wild-type embryo heads, almost 70% of the S-phase population was in early S-phase. Intriguingly, the

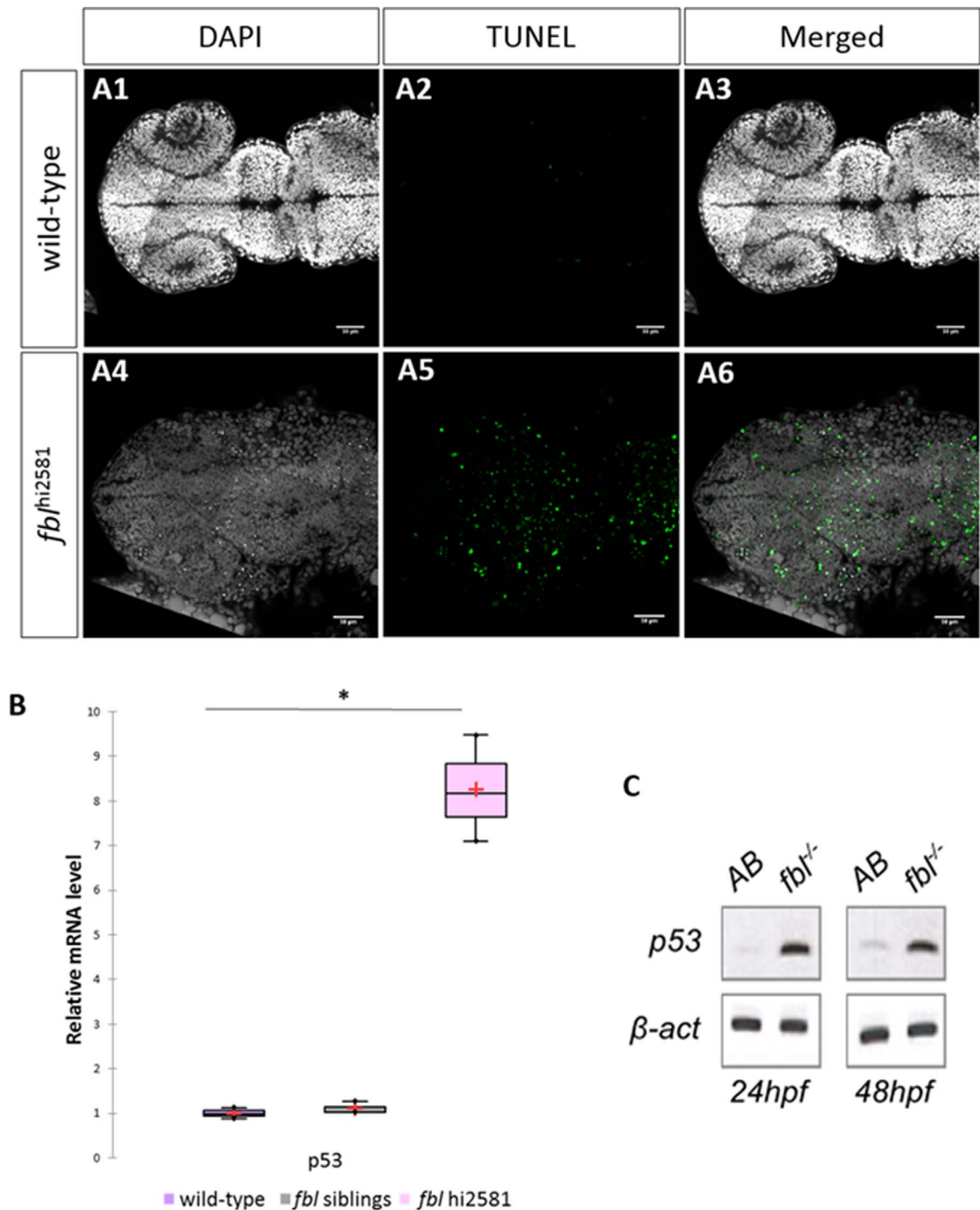


Fig. 7. Massive p53-dependent apoptosis in the *fbl* mutant. **(A)** Horizontal optic sections of TUNEL labeling at 24 hpf in wild-type (**A1-A3**) and mutant (**A4-A6**) embryos. Gray: DAPI staining, Green: TUNEL staining. Scale bar: 50 µm. Anterior is to the left. **(B)** RT-qPCR quantification of relative levels of *tp53* mRNA at 72 hpf shows a strong increase in *tp53* expression in mutants. Purple: wild-type, gray: siblings, pink: mutants. Statistical analyses were performed on biological triplicates, *p*-value (Kruskal-Wallis test): 0.049. **(C)** RT-PCR for *tp53* in 24 hpf and 48 hpf mutant embryos showing a large increase in *tp53* expression. Anterior is to the left.

proportion of S-phase cells in early S phase was lower (50%) in mutant head cells. By contrast, the proportions of mutant cells in the mid- and late S phases were higher than those for wild-type cells (Fig. 9D). Indeed, 18% of wild-type cells were in mid-S phase and 12% were in late S-phase, whereas the corresponding proportions for mutant cells were 28% and 20%.

We investigated the alterations of S-phase in *fbl* mutants further, by evaluating the level of expression of *cdkn1a* (also called *p21^{waf1}*), the product of which is involved in both the regulation of G1 progression

and S-phase DNA replication and accumulates during DNA damage repair (Li et al., 1994). Levels of *cdkn1a* expression were markedly higher in mutant embryos than in control and sibling embryos at 3 dpf (Fig. 9E). This suggests that the progression of DNA replication in S-phase is disturbed in the mutant larvae.

3. Discussion

The goal of this study was to investigate the role of Fbl in cell

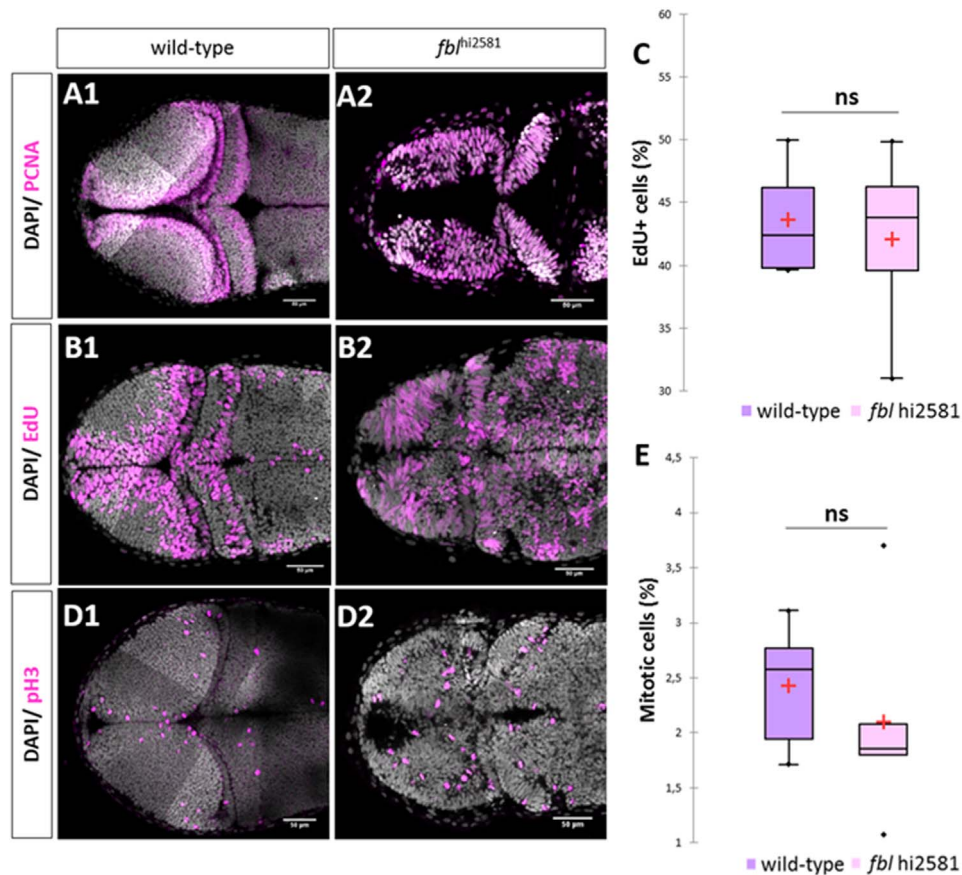


Fig. 8. In *fbl* mutants, the S-phase of the cell cycle is affected. **(A)** PCNA staining in 2dpf wild type **(A1)** and mutant **(A2)**. In wild-type larvae, proliferative cells were restricted to the periphery of each tectal lobes. In *fbl*^{hi2581Tg} PCNA positive cells were observed in almost all tectal cells. **(B)** EdU incorporation experiments in 2dpf wild type **(A1)** and mutant **(A2)** embryos after two hour pulse. In wild-type embryos, EdU-positive cells are restricted to the periphery of the OT while in the *fbl*^{hi2581Tg} mutant embryos EdU-positive cells are spread all over the structure. **(C)** EdU-positive cells quantification in wild-type (purple) and mutant (pink) embryos at 2dpf. Statistical analyzes have been performed on four samples per conditions, p-value (Mann & Whitney test): 1.00. **(D)** pH3 staining in 2dpf wild types **(E1)** and mutants **(E2)** embryos. Similar abnormal patterns in mutants as for EdU incorporation experiments. **(E)** pH3-positive cells quantification in wild-type (purple) and mutant (pink) embryos at 2dpf. Statistical analyzes have been performed on four samples per conditions, p-value (Mann & Whitney test): 0.53 **(E)** embryos. Gray: DAPI staining, Pink: EdU, pH3 or PCNA staining. Scale bar: 50 μ m. Anterior is to the left.

homeostasis *in vivo* in a vertebrate model. A convenient feature of zebrafish is the ease of studying mutant embryogenesis during early development due to the availability of maternal supplies. In the mouse, homozygous depletion of fibrillarin leads to death prior to implantation (Newton et al., 2003). In zebrafish mutants, defects occur later, after gastrulation and during somitogenesis. The large maternal stocks of mature ribosomes and RBFs present in the zebrafish oocyte is used up during the first day after fertilization (Azuma et al., 2006).

First, in the mutant used in this study, we checked by RT-qPCR the loss of *fbl* expression. No *fbl* transcript could be detected as early as the 24 hpf stage. We also checked that the injection of *fbl* mRNA rescued the mutant phenotype. It is noteworthy that mutations in genes encoding Nop56 and Nop58, two core proteins of the C/D box complex led to the same developmental defects (*nop56*^{hi3101Tg} and *nop58*^{hi3118Tg}, ZFIN).

3.1. Why are the defects of fibrillarin mutants mostly found in the tectum and the eyes?

We show here that Fbl is preferentially expressed in slow-amplifying progenitors (SAPs) of the retina (CMZ) and tectum (TMZe). However, the Fbl protein is not totally absent from differentiated cells and fast-amplifying progenitors (FAPs), but present in various amounts in the different cell types of the OT and retina.

fbl mutant embryos are hypomorphic, particularly for the brain and eye. We also observed severe cellular hypoplasia and an impairment of neuronal differentiation and specification specifically in the dorsal

midbrain and in retina.

An explanation why the dorsal midbrain and eyes are severely affected is linked to the differences in the kinetics of development between the dorsal midbrain and other more posterior or ventral regions. Neurogenesis begins earlier in the ventral part of the brain. After the completion of neural differentiation in the ventral regions, the dorsal part of the brain, including the OT, continues to produce neurons to support its specific sustained growth (Joly et al., 2016). The ventral and dorsal midbrain neural cells may therefore be affected differently by the lack of Fbl.

Despite the specific accumulation of Fbl in the SAPs of the TMZe, these cells are not strongly affected, as they continue to divide, display little apoptosis and the neuroepithelial layer connecting the OT to the TS (Recher et al., 2013) seems to be unaffected in mutants (although it is somewhat thicker). Since TMZe progenitors cycle at a lower rate than TMZi cells (Recher et al., 2013), they may remain protected until later in development. In these cells, the dilution of maternal stocks of ribosomes or of correctly methylated ribosomes may be slower than in more actively dividing cells.

By contrast, the FAPs are profoundly disturbed and they have a different distribution, with a massive presence in the center of the tectum at 3 dpf in mutants, whereas these cells are peripheral in the wild type. There are at least two possible reasons for this difference of localization of progenitors. First, *fbl* loss of function could lead to a developmental delay, as proliferative cells are found throughout the entire structure at earlier stages. Another most likely hypothesis is that the *fbl* mutation may lead to cell cycle deregulation due to the rapid

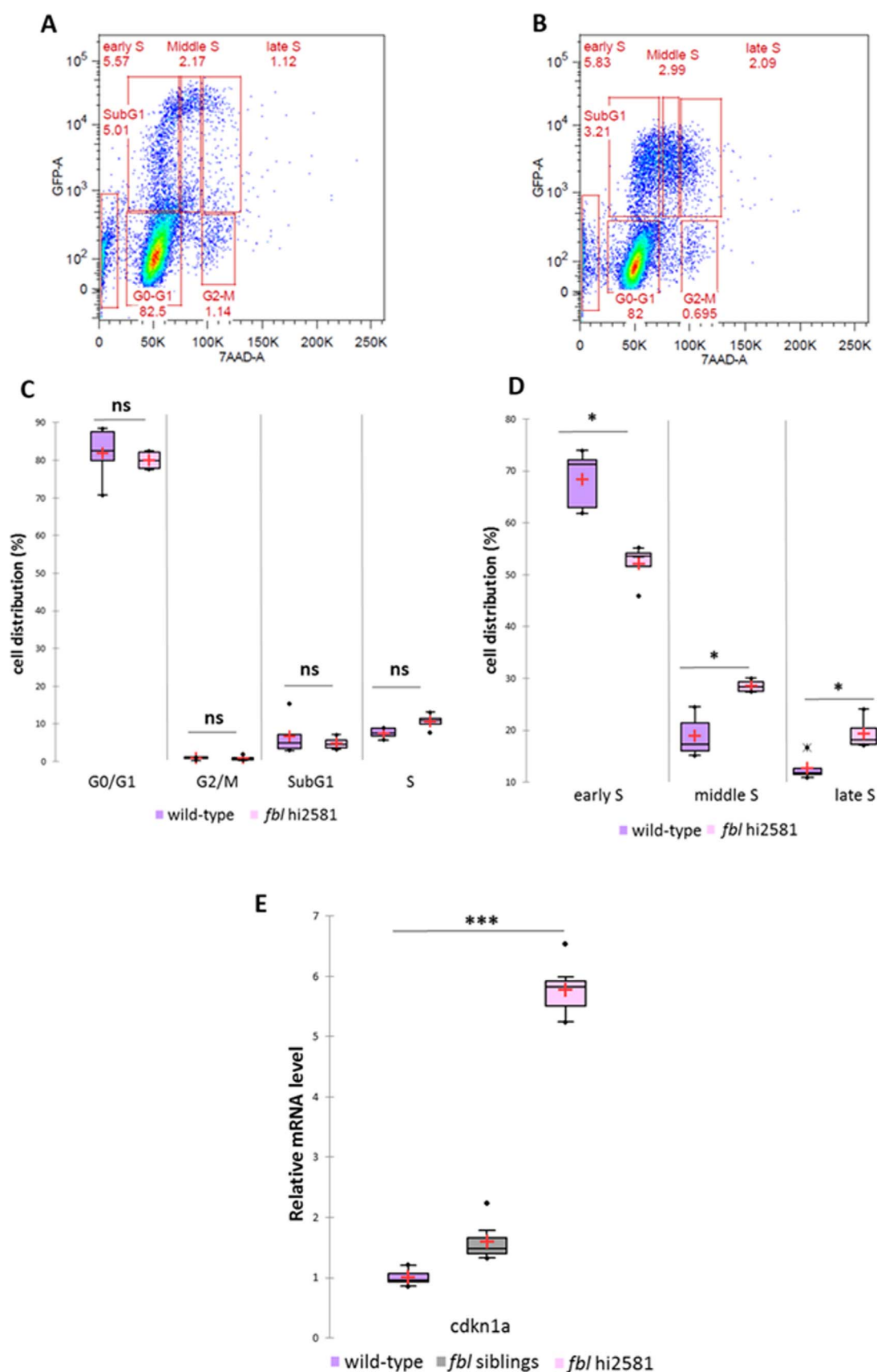


Fig. 9. S-phase progression is altered in *fbl* mutant embryos. **(A-B)** FACS analyses of 3 dpf wild-type and mutant heads after a two-hour pulse of EdU. DNA content was assessed by labeling with 7-AAD. **(C-D)** Quantification and analysis of the distribution of the cells in the different phases of the cell cycle. Statistical analyses were performed on five replicates for the wild-type embryos and four for the mutant embryos, *p*-values (Mann & Whitney test): subG1 = 0.903; G0/G1 = 0.461; S = 0.066; G2/M = 0.713; Early S = 0.016; Mid-S = 0.016; Late S = 0.016. **(E)** RT-qPCR quantification of relative levels of mRNA for *cdkn1a* at 3 dpf showing higher levels of *cdkn1a* expression in mutants, consistent with an alteration of DNA replication. Statistical analyses were performed on biological triplicates, *p*-value (Mann & Whitney test): 0.027. Purple: wild-type, gray: siblings, pink: mutants.

dilution of maternal components in these cells. In favor of this hypothesis, we observed that in *fbl* mutants, S-phase progression was disrupted.

In human, ribosomopathies, a group of diseases associated with defects in ribosome biogenesis, display tissue specificity and variability in their clinical manifestations (Danilova and Gazda, 2015). In zebrafish models of ribosomopathies, tissues the most affected are the ones with high rate of proliferation (brain, eye, intestine, hematopoietic lineage...).

3.2. Potential consequences of the impairment of ribosome biogenesis and translational activity in *fbl* mutants

Fbl is the methyltransferase of the box C/D complex. It is responsible for the methylation of both rRNA and histones associated with rDNA loci. An absence of Fbl or low levels of this protein lead to abnormally low levels of rDNA transcription and changes of the posttranscriptional modification of rRNAs (Erales et al., 2017).

We show here, *in vivo*, that *fbl* mutants display impaired ribosome biogenesis, and, more particularly, low levels of ribosome activity, as illustrated by the low proportion of polysomes. This finding may be explained by translation initiation defects. Indeed, we observed no change in the size of the 80 S peak, corresponding to the binding of one ribosome to the target mRNA. We also found that 18 S rRNA levels were much lower in *fbl*^{hi2581Tg} mutant embryos than in the wild type, strongly suggesting that the last steps of the ribosome biogenesis pathway are impaired. Therefore it seems likely that the ribosomes can bind to mRNA, but that the translation initiation defects prevent the binding of other ribosomes. However, it remains possible that a feedback loop detects the decrease in translation and subsequently decreases the rates of formation of the two subunits.

The lower level of ribosome activity may be due to lower levels of rRNA methylation, resulting in a lower affinity for specific mRNA targets. Indeed, using RiboMethSeq, it has recently been shown that FBL knockdown in human cells led to modification of 2'-O-methylation on functional domains of ribosomes (Erales et al., 2017).

We also suggest that Fbl may accumulate specifically in SAPs for the production of different ribosomes responsible for the translation of specific targeted mRNAs. Indeed, many RBF-coding genes have tissue-specific patterns of expression in zebrafish (Brombin et al., 2015). In particular, rRNA post-transcriptional modifications and ribosomal protein contents differ between the ribosomes of different cell types, particularly between stem and progenitor cells (Brombin et al., 2015). Moreover, different types of rRNAs are produced in oocytes and during zebrafish development (Locati et al., 2017). Kraushar et al. recently suggested that ribosomes drive the spatiotemporal development of the neocortex (Kraushar et al., 2016). This hypothesis is based on the putative existence of a progenitor-specific ribosome signature during brain development, highlighting the tissue specificity of ribosome biogenesis.

3.3. Why is S-phase progression disrupted in *fbl* mutant embryos?

As mentioned above, there are several compelling lines of evidence suggesting that cell division is disturbed in *fbl* mutants. The impairment of ribosome biogenesis often leads to disturbance of the cell cycle (Xu et al., 2016), and cells are often arrested at the G1/S transition (James et al., 2014) or, in rarer cases, at the G2/M checkpoint (Fumagalli et al., 2012; Negi and Brown, 2015).

Surprisingly, FACS analysis of *fbl*^{hi2581Tg} mutant cells revealed that the mutant cells were not blocked at the G1/S or G2/M checkpoints, but that they progressed through the cell cycle, as the distribution of cells in the different phases of the cell cycle was similar to that for wild-type cells (Xu et al., 2016).

However, the distribution of cells in the various parts of S-phase was disrupted in *fbl*^{hi2581Tg} mutants, suggesting a delay in S-phase and in the

replication fork progression. The observed distributions on FACS analysis of mutant and wild-type cells suggests that replication origins normally activated early in S phase might be activated later in S phase in mutant cells. The low intensity of EdU incorporation is consistent with this hypothesis. The genomic material is replicated during S-phase, for subsequent mitosis. The impairment of pre-rRNA processing might interfere with transcription and, ultimately, with DNA replication (Bermejo et al., 2012). S-phase progression is tightly regulated by the replication timing process (Lucas and Feng, 2003; Mendez, 2009; Fragkos et al., 2015; Zink, 2006). In particular, the tight regulation of replication timing facilitates the sequential activation of replication origins during S-phase. We suggest that, in the absence of Fbl, the lower levels of ribosomal translation activity due to the disruption of ribosome biogenesis, delay or decrease the translation of many proteins. In particular, proteins involved in DNA replication and origin firing could be lacking, preventing the correct timing of DNA replication and leading to replication stress and genomic instability.

We also observed higher levels of p21^{waf1} expression in mutant cells. In addition to its role in cell cycle exit, p21^{waf1} accumulation leads to a DNA replication block and cell cycle arrest in S-phase (Li et al., 1994; Waga et al., 1994). This protein accumulates when DNA is damaged. The observed accumulation of *tp53* transcripts is also consistent with the presence of DNA breaks. These findings suggest that the intra-S defects in *fbl*^{hi2581Tg} embryos may be linked not only to defective replication, but also to the presence of DNA damage, resulting in replication stress. Other nucleolar proteins, such as nucleostemin, have been implicated in both ribosome biogenesis, and the maintenance of genome integrity.

Further studies are required to deepen our understanding of the origin of the tissue-specific intra-S defects in *fbl* mutants. Such studies should also provide insight into the tissue-specific defects observed in ribosomopathies (Yelick and Trainor, 2015).

4. Material and methods

4.1. Zebrafish lines and husbandry

We used the following *Danio rerio* lines for this work: wild-type strain AB and *fbl*^{hi2581Tg} mutants (ZIRC, Eugene, OR, USA). All zebrafish lines were maintained at 28 °C in our facility. Embryos were kept at 28 °C and staged as described by Kimmel (Kimmel et al., 1995). *fbl*^{hi2581Tg} adult zebrafish were maintained as heterozygotes and inbred to generate homozygous mutant embryos. PCR was conducted on adults, to check for the presence of the insertional mutation. The wild-type *fbl* allele was detected with the following primers: forward 5'-GAGGAAAAGCGGGTCTGAG-3' and reverse 5'-AGTGCCTGGC-TAACTCATCC-3'. The *fbl* mutant allele was detected with the following primers: forward 5'-GAGGAAAAGCGGGTCTGAG-3' and reverse 5'-GAAGCCTATAGGTACGAGCCATAG-3'. All procedures were performed in accordance with European Union Directive 2011/63/EU.

4.2. mRNA synthesis and injection

cDNA full length encoding for zebrafish Fbl was cloned into pCS2 + vector. Fbl-PCS2 plasmid was linearized with Kpn1 endonuclease (New England Biolabs) and used for the *in vitro* synthesis of mRNAs by the mMESSAGE mMACHINE T3 Transcription Kit (Life Technologies). Purified *fbl* mRNA (60, 100, 200 pg/embryo) was injected into one-cell stage embryos of *fbl*^{hi2581Tg} heterozygous in cross progeny.

4.3. Immunohistochemistry

Whole-mount immunohistochemistry (WMIHC) was performed as previously described (Inoue and Wittbrodt, 2011). Embryos were first incubated in a depigmentation solution (0.5 × SSC/5%formamide/3%

H₂O₂) at room temperature for 30 min. WMIHC for PCNA was performed specifically, with the fast protocol of the Tefor Core Facility (<http://tcf.tefor.net>; unpublished protocol): following depigmentation, embryos were incubated in unmasking solution (HistoVT One, 06980–05, Nacalai Tesque) at 68 °C for 1 h. Blocking and permeabilization (10% NGS, 10% DMSO, 5% PBS-1 M glycine, 0.5% Triton X-100, 0.1% Tween 20, 0.1% sodium deoxycholate, 0.1% NP40) were performed simultaneously over a period of five hours. The embryos were incubated with antibodies for three days at 4 °C, in staining solution (2% NGS, 20% DMSO, 10 µg/ml heparin, 0.2% Triton X-100, 1 × PBS, 0.1% Tween 20, 0.05% sodium azide).

We used mouse anti-PCNA (Dako, 1:150), human anti-FBL (1:1000, autoimmune serum, gift from Danièle Hernandez-Verdun, Jacques Monod Institute, Paris France), rabbit anti-pH3 (Millipore, 1:500) and mouse anti-elavl3 (Molecular Probes, Life Technologies, 1:100) primary antibodies.

The fluorescent secondary antibodies used for detection were AlexaFluor 488- or AlexaFluor 555-conjugated goat anti-rabbit, goat anti-mouse or goat anti-human antibodies (1:200, Molecular Probes, Life Technologies).

4.4. EdU labeling

We injected 1 nl of 5-ethynyl-2'-deoxyuridine (EdU, 10 mM, Molecular Probes, Life Technologies) into the pericardiac cavity of 48 hpf and 72 hpf wild-type and mutant embryos, which were fixed two hours later. EdU was detected with the EdU Click-iT Plus EdU Alexa Fluor 488 or 647 Imaging kit (Molecular Probes, Life Technologies), according to the manufacturer's protocol.

4.5. TUNEL staining

TUNEL labeling was performed with the Deadend Fluorometric TUNEL system (Promega), according to manufacturer's instructions. Embryos were washed in PBS, counterstained with DAPI (Sigma) and mounted in Vectashield hard-set mounting medium (Vector Laboratories).

4.6. Whole-mount *in situ* hybridization

Riboprobes were synthesized as follows: cDNA (PCR-amplified with specific primers was inserted into a pCR II-TOPO vector (Molecular Probes). The sequence and orientation of the inserts were checked by direct sequencing (GATC Biotech). The products of PCR amplification of the inserts with generic SP6-T7 primers were used to synthesize the antisense riboprobes, with T7 or SP6 polymerase (Promega) (chosen on the basis of the sequencing results). Digoxigenin (DIG)-conjugated probes were synthesized with the UTP-DIG nucleotide mix (Roche) and purified with RNA clean-up kit (Macherey-Nagel).

Whole-mount *in situ* hybridization was performed on manually staged (according to Kimmel et al., 1995) dechorionated PTU-treated embryos fixed in 4% paraformaldehyde (PFA)/phosphate-buffered saline (PBS) and stored in methanol at –20 °C. Briefly, embryos stored in methanol were rehydrated in a methanol/PBS series, permeabilized with proteinase K (10 mg/ml), prehybridized, and then hybridized overnight at 65 °C in hybridization mixture (HM: 50% formamide, 5 × standard saline citrate (SSC), 0.1% Tween 20, 100 mg/ml heparin, 100 mg/ml tRNA in water). The embryos were subjected to a series of washes in 50% SSC/formamide and SSC/PBST, and were then incubated in blocking solution for one hour (0.2% Tween 20, 0.2% Triton X-100, 2% sheep serum in PBST) and overnight at 4 °C with AP-conjugated anti-DIG antibodies (Roche) diluted 1:4000 in blocking solution. Embryos were then washed in PBST, soaked in staining buffer (TMN: 100 mM NaCl, 100 mM Tris-HCl, pH 9.5, 0.1% Tween 20 in water) and incubated in NBT/BCIP (nitroblue tetrazolium/5-bromo-4-chloro-3-indolyl phosphate) solution (Roche).

4.7. Cresyl violet staining

PFA-fixed embryos were dehydrated in ethanol solutions of increasing concentration and incubated in butanol before embedding in paraffin. Serial sections were prepared with a Leica rotary microtome and mounted on glass slides according to standard procedures, then stained with a cresyl violet-thionine solution.

4.8. Imaging

Bright-field imaging was performed with a Nikon AZ100 macro-scope (Camera: Nikon Digital Sight DSRI1; Objectives: AZ-Plan Fluor 5 × (O.N.: 0.5/D.T.: 15 mm)). Fluorescence imaging was performed using a confocal laser scanning microscope (Leica SP8) with internal photomultiplier tubes (Airy: 1; Objectives: Fluotar VISIR 25 × /0.95 WATER; Plan-APOCHROMAT 40 × /1.10 WATER).

4.9. Segmentation

The 3D-visualization and segmentation of zebrafish specimens were generated using 3D Slicer 4 (Fedorov et al., 2012) on a HP computer with a 2.9 GHz Intel Core i7–4910MQ CPU and 32 Gb of RAM.

To first obtain global larva shape, we performed 3D visualization of DiI-staining using the volume rendering module of 3D Slicer which transforms brightness values into opacity values. Using this module, we rendered dark voxels transparent, bright voxels more opaque.

Prior to segmentation, we downsampled the data to a voxel size of 3.5 × 3.5 × 3.5 µm using the python script SimpleITK (Lowekamp et al., 2013) and NumPy.

We segmented the patterns of interest using the segment editor module of 3D Slicer. The nervous system was segmented using the DiI channel by applying a manual threshold and refining the segmentation with the paint and erase tools, restricting it to eyes and brain. Due to its high specificity, this correction step was not necessary for Elavl3-staining pattern and a similar segmentation strategy was applied. For label smoothing, we subsequently applied a median filter of 5 × 5 × 5 voxels.

We visualized segmentations with a surface rendering, using the Create surface function of the Segment editor module of 3D Slicer. For each segmentation, we generated a label map volume, counted the number of voxels and computed the volume for each by multiplying the number of voxels by the size of a voxel.

4.10. Quantitative real-time PCR

Total RNA was extracted from 72 hpf zebrafish embryos in TRIzol reagent (Invitrogen), purified and treated with DNase, with the Macherey Nagel NucleoSpin® RNAII kit. RNA was quantified with a Nanodrop 2000c spectrophotometer (Thermo Scientific) and the integrity of the RNAs was checked with an Agilent 2100 bioanalyzer and the eukaryote total RNA Nano assay (Agilent Technologies). We reverse-transcribed 1 µg of total RNA in a final reaction volume of 20 µl, with the High Capacity cDNA Reverse Transcription Kit (Life Technologies), RNase inhibitor and random primers, according to the manufacturer's instructions. Quantitative PCR was performed on a QuantStudio™ 12 K Flex Real-Time PCR System with a SYBR green detection protocol. We mixed 1.5 ng of cDNA with Fast SYBR® Green Master Mix and 500 nM of each primer, in a final volume of 10 µl. The reaction mixture was subjected to 40 cycles of PCR (95 °C/20 s; [95 °C/1 s; 60 °C/20 s] X40) followed by a fusion cycle, for analysis of the melting curve of the PCR products. Negative controls without reverse transcriptase were introduced, to check for the absence of genomic DNA contaminants. Primers were designed with the Primer-Blast tool from NCBI and Primer Express 3.0 software (Life Technologies). With

the exception of the ribosomal primers, the primers used bound to one exon and one exon-exon junction. Specificity and the absence of multi-locus matching at the primer site were checked by BLAST analysis. The amplification efficiencies of primers were determined from the slopes of standard curves generated with a four-fold dilution series. The amplification specificity of each real-time PCR was confirmed by analyzing the dissociation curves. The Ct values obtained were then used for further analyses, with the *gapdh*, *actb1* and *thp* genes as references. Each sample was assessed at least in duplicate.

The primers used were as follows:

<i>gapdh-F</i>	TTAACGGATTTCGGTCGCATT
<i>gapdh-R</i>	CCGCCTTCTGCCTTAACCTC
<i>actb1-F</i>	TACACAGCCATGGATGAGGAAAT
<i>actb1-R</i>	TCCCTGATGTCTGGGTCGTC
<i>thp-F</i>	ATCTCCACAGGGAGCCATGA
<i>thp-R</i>	CAGGAGGGACAAGCTGTTGG
<i>fbl-F</i>	GAGGATGCTCTGGTCACAAAG
<i>fbl-R</i>	CTGAAAGGATTCCACGCTCT
<i>5'ETS-F</i>	CCGGTCTACCTCGAAAGTC
<i>5'ETS-R</i>	CGAGCAGAGTGGTAGAGGAAG
<i>ITS1-F</i>	CTCGGAAAACGGTGAACCTG
<i>ITS1-R</i>	GTGTTCTGTTTCAGGGTCCG
<i>ITS2-F</i>	CCTAAGCGCAGACCGT
<i>ITS2-R</i>	AGCGCTGGCCTCGGAGATC
<i>18S-F</i>	ACACGGGGAGGTAGTGACGA
<i>18S-R</i>	TCGCCCATGGGTTTAGGATA
<i>tp53-F</i>	GAACCCCGGATGGAGATAACTT
<i>tp53-R</i>	CAGTTGTCCATTACAGACCAAG
<i>neurod1-F</i>	CAACACACCCTAGAGTTCGACAT
<i>neurod1-R</i>	CCACGTCTCGTTCGTTCTGG
<i>cdkn1a-F</i>	TTCGAGAAGCTCAAAACATATTGTC
<i>cdkn1a-R</i>	ACGCAAAGTCGAAGCTCCAG

4.11. Polysome profile

We collected 60 wild-type and 100 mutant embryos per sample at 3dpf. Embryos were deyolked, rinsed with ice-cold PBS and dissociated in ice-cold lysis buffer (10 mM Tris-HCl, 5 mM MgCl₂, 100 mM KCl, 1% Triton-X100, 2 mM DTT, 100 µg/ml cycloheximide, 200 U/ml RNasin (Promega), and protease inhibitor (Sigma)). Dissociated cells were subjected to sucrose gradient centrifugation (31% sucrose, 50 mM Tris-acetate pH 7.6, 50 mM NH₄Cl, 12 mM MgCl₂, 1 mM DTT). Gradients were successively frozen and thawed before use. The gradients were then centrifuged for 3 h in an SW41 rotor (4 °C, 39,000 rpm) and fractionated with the ISCO system.

4.12. Cell dissociation and FACS

Injection of 1 nL of EdU (10 µM) was first performed in pericardial space of embryos. Following EdU incorporation, embryos were placed in ice-cold embryo medium (5.03 mM NaCl, 0.17 mM KCl, 0.33 mM CaCl₂·2H₂O, 0.33 mM MgSO₄·7H₂O) for 10 min and transferred to ice-cold Ringer solution for 10 min. The tails and bodies of the embryos were removed and the heads were placed in 500 µl of FACSMAX (Manoli and Driever, 2012). Cells were dissociated by manual squishing of the embryos cell strainer (with 40-µm mesh). Cells were collected by centrifugation (500 × g, 10 min, 4 °C) of the suspensions, and fixed by incubation in ethanol 70% at – 20 °C for 2 days. EdU was detected as described in the “EdU labeling” section. Cells were then incubated in PBS buffer containing 0.1% Triton X-100, RNase A (SIGMA, 0.5 µg/ml) and 7-AAD (BD Pharmingen 559925, 20 µl in 1 ml buffer), and then incubated for 1 h in the dark at 37 °C before flow cytometry analysis. DNA content was assessed with a BD FACSCalibur analyzer and analyses were performed with FlowJo software.

4.13. Statistical analyses

Statistical analysis was performed with Microsoft Excel XLSTAT software. All data are expressed as means ± standard deviations. We calculated two-tailed *p*-values for Kruskal-Wallis non-parametric tests with Bonferroni correction for comparisons between three groups, and Mann-Whitney tests for comparisons of two groups.

Acknowledgments

We wish to thank Julien Hemon, Arnim Jennet, Elodie Machado and Laurie Rivière (Tefor Core Facility) and Charlene Lasgi (Curie Institute, flow cytometry platform) for technical assistance; Pierre Affaticati (Tefor Core Facility), Odile Bronchain (NeuroPsi), Jean-Michel Hermel and Aurélie Heuzé (CASBAH group), Olivier Namy (I2BC), Vincent Pennaneach (Curie Institute) for fruitful discussion and Frédéric Catez (CRCL) for sharing unpublished data. This work has benefited from the facilities and expertise of TEFOR (TEFOR Infrastructure - Investissement d'avenir - ANR-II-INBS-0014). This research received financial support from the FINEST project (ANR-11-BSV2-0029), INRA PHASE department and from a grant of the “Fondation Leducq”. Stéphanie Bouffard acknowledge the receipt of MENESR (French minister) fellowship.

Author contributions

Stéphanie Bouffard and Françoise Jamen: Conception and design, Collection and assembly of data, Data analysis and interpretation, manuscript writing and manuscript proof reading; Alessandro Brombin and Emilie Dambroise: conception and design, Collection and assembly of data, Data analysis and interpretation; Sylvain Lempereur, Isabelle Hatin and Raphaël Corre: Collection and assembly of data; Franck Bourrat and Matthieu Simion: Data analysis and interpretation and manuscript proof reading; Jean-Stéphane Joly: Conception and design, Data analysis and interpretation and manuscript proof reading.

References

- Affaticati, P., Yamamoto, K., Rizzi, B., Bureau, C., Peyrieras, N., Pasqualini, C., Demarque, M., Vernier, P., 2015. Identification of the optic recess region as a morphogenetic entity in the zebrafish forebrain. *Sci. Rep.* 5, 8738.
- Amin, M.A., Matsunaga, S., Ma, N., Takata, H., Yokoyama, M., Uchiyama, S., Fukui, K., 2007. Fibrillarin, a nucleolar protein, is required for normal nuclear morphology and cellular growth in HeLa cells. *Biochem. Biophys. Res. Commun.* 360, 320–326.
- Amsterdam, A., Nissen, R.M., Sun, Z., Swindell, E.C., Farrington, S., Hopkins, N., 2004. Identification of 315 genes essential for early zebrafish development. *Proc. Natl. Acad. Sci. USA* 101, 12792–12797.
- Azuma, M., Toyama, R., Laver, E., Dawid, I.B., 2006. Perturbation of rRNA synthesis in the bap28 mutation leads to apoptosis mediated by p53 in the zebrafish central nervous system. *J. Biol. Chem.* 281, 13309–13316.
- Brombin, A., Joly, J.S., Jamen, F., 2015. New tricks for an old dog: ribosome biogenesis contributes to stem cell homeostasis. *Curr. Opin. Genet. Dev.* 34, 61–70.
- Choi, Y.W., Kim, Y.W., Bae, S.M., Kwak, S.Y., Chun, H.J., Tong, S.Y., Lee, H.N., Shin, J.C., Kim, K.T., Kim, Y.J., Ahn, W.S., 2007. Identification of differentially expressed genes using annealing control primer-based GeneFishing in human squamous cell cervical carcinoma. *Clin. Oncol. (R. Coll. Radiol.)* 19, 308–318.
- Danilova, N., Gazda, H.T., 2015. Ribosomopathies: how a common root can cause a tree of pathologies. *Dis. Model. Mech.* 8, 1013–1026.
- Deves, M., Bourrat, F., 2012. Transcriptional mechanisms of developmental cell cycle arrest: problems and models. *Semin. Cell Dev. Biol.* 23, 290–297.
- Erales, J., Marchand, V., Panthou, B., Gillot, S., Belin, S., Ghayad, S.E., Garcia, M., Laforets, F., Marcel, V., Baudin-Baillieu, A., Bertin, P., Coute, Y., Adrait, A., Meyer, M., Therizols, G., Yusupov, M., Namy, O., Ohlmann, T., Motorin, Y., Catez, F., Diaz, J.J., 2017. Evidence for rRNA 2'-O-methylation plasticity: control of intrinsic translational capabilities of human ribosomes. *Proc. Natl. Acad. Sci. USA* 114, 12934–12939.
- Fedorov, A., Beichel, R., Kalpathy-Cramer, J., Finet, J., Fillion-Robin, J.C., Pujol, S., Bauer, C., Jennings, D., Fennessy, F., Sonka, M., Buatti, J., Aylward, S., Miller, J.V., Pieper, S., Kikinis, R., 2012. 3D slicer as an image computing platform for the quantitative imaging network. *Magn. Reson. Imaging* 30, 1323–1341.
- Fragkos, M., Ganier, O., Coulombe, P., Mechali, M., 2015. DNA replication origin activation in space and time. *Nat. Rev. Mol. Cell Biol.* 16, 360–374.
- Fumagalli, S., Ivanenkov, V.V., Teng, T., Thomas, G., 2012. Suprainduction of p53 by

- disruption of 40S and 60S ribosome biogenesis leads to the activation of a novel G2/M checkpoint. *Genes Dev.* 26, 1028–1040.
- Inoue, D., Wittbrodt, J., 2011. One for all – a highly efficient and versatile method for fluorescent immunostaining in fish embryos. *PLoS ONE* 6, e19713.
- James, A., Wang, Y., Raje, H., Rosby, R., DiMario, P., 2014. Nucleolar stress with and without p53. *Nucleus* 5, 402–426.
- Joly, J.S., Recher, G., Brombin, A., Ngo, K., Hartenstein, V., 2016. A conserved developmental mechanism builds complex visual systems in insects and vertebrates. *Curr. Biol.* 26, R1001–R1009.
- Kimmel, C.B., Ballard, W.W., Kimmel, S.R., Ullmann, B., Schilling, T.F., 1995. Stages of embryonic development of the zebrafish. *Dev. Dyn.* 203, 253–310.
- Koh, C.M., Iwata, T., Zheng, Q., Bethel, C., Yegnasubramanian, S., De Marzo, A.M., 2011. Myc enforces overexpression of EZH2 in early prostatic neoplasia via transcriptional and post-transcriptional mechanisms. *Oncotarget* 2, 669–683.
- Kraushar, M.L., Popovitchenko, T., Volk, N.L., Rasin, M.R., 2016. The frontier of RNA metamorphosis and ribosome signature in neocortical development. *Int. J. Dev. Neurosci.* 55, 131–139.
- Laferte, A., Favry, E., Sentenac, A., Riva, M., Carles, C., Chedin, S., 2006. The transcriptional activity of RNA polymerase I is a key determinant for the level of all ribosome components. *Genes Dev.* 20, 2030–2040.
- Le Bouteiller, M., Souilhols, C., Beck-Cormier, S., Stedman, A., Burlen-Defranoux, O., Vandormael-Pournin, S., Bernex, F., Cumano, A., Cohen-Tannoudji, M., 2013. Notchless-dependent ribosome synthesis is required for the maintenance of adult hematopoietic stem cells. *J. Exp. Med.* 210, 2351–2369.
- Li, R., Waga, S., Hannon, G.J., Beach, D., Stillman, B., 1994. Differential effects by the p21 CDK inhibitor on PCNA-dependent DNA replication and repair. *Nature* 371, 534–537.
- Locati, M.D., Pagano, J.F.B., Girard, G., Ensink, W.A., van Olst, M., van Leeuwen, S., Nehrdich, U., Spaink, H.P., Rauwerda, H., Jonker, M.J., Dekker, R.J., Breit, T.M., 2017. Expression of distinct maternal and somatic 5.8S, 18S, and 28S rRNA types during zebrafish development. *RNA* 23, 1188–1199.
- Loweckamp, B.C., Chen, D.T., Ibanez, L., Blezek, D., 2013. The Design of SimpleITK. *Front. Neuroinform.* 7, 45.
- Lucas, I., Feng, W., 2003. The essence of replication timing: determinants and significance. *Cell Cycle* 2, 560–563.
- Ma, T.H., Lee, L.W., Lee, C.C., Yi, Y.H., Chan, S.P., Tan, B.C., Lo, S.J., 2016. Genetic control of nucleolar size: an evolutionary perspective. *Nucleus* 7, 112–120.
- Manoli, M., Driever, W., 2012. Fluorescence-activated cell sorting (FACS) of fluorescently tagged cells from zebrafish larvae for RNA isolation. *Cold Spring Harb. Protoc.* 2012.
- Marcel, V., Catez, F., Diaz, J.J., 2013. p53, a translational regulator: contribution to its tumour-suppressor activity. *Oncogene* 34, 5513–5523.
- Mendez, J., 2009. Temporal regulation of DNA replication in mammalian cells. *Crit. Rev. Biochem. Mol. Biol.* 44, 343–351.
- Mullineux, S.T., Lafontaine, D.L., 2012. Mapping the cleavage sites on mammalian pre-rRNAs: where do we stand? *Biochimie* 94, 1521–1532.
- Negi, S.S., Brown, P., 2015. rRNA synthesis inhibitor, CX-5461, activates ATM/ATR pathway in acute lymphoblastic leukemia, arrests cells in G2 phase and induces apoptosis. *Oncotarget* 6, 18094–18104.
- Newton, K., Petfalski, E., Tollervey, D., Caceres, J.F., 2003. Fibrillarin is essential for early development and required for accumulation of an intron-encoded small nucleolar RNA in the mouse. *Mol. Cell. Biol.* 23, 8519–8527.
- Nguyen, V., Deschet, K., Henrich, T., Godet, E., Joly, J.S., Wittbrodt, J., Chourrout, D., Bourrat, F., 1999. Morphogenesis of the optic tectum in the medaka (*Oryzias latipes*): a morphological and molecular study, with special emphasis on cell proliferation. *J. Comp. Neurol.* 413, 385–404.
- Recher, G., Jouralet, J., Brombin, A., Heuze, A., Mugniery, E., Hermel, J.M., Desnoullez, S., Savy, T., Herbomel, P., Bourrat, F., Peyrieras, N., Jamen, F., Joly, J.S., 2013. Zebrafish midbrain slow-amplifying progenitors exhibit high levels of transcripts for nucleotide and ribosome biogenesis. *Development* 140, 4860–4869.
- Rodriguez-Corona, U., Sobol, M., Rodriguez-Zapata, L.C., Hozak, P., Castano, E., 2015. Fibrillarin from Archaea to human. *Biol. Cell* 107, 159–174.
- Schimmg, F., Tollervey, D., Kern, H., Frank, R., Hurt, E.C., 1989. A yeast nucleolar protein related to mammalian fibrillarin is associated with small nucleolar RNA and is essential for viability. *Embo J.* 8, 4015–4024.
- Shubina, M.Y., Musinova, Y.R., Sheval, E.V., 2016. Nucleolar Methyltransferase Fibrillarin: evolution of Structure and Functions. *Biochemistry (Moscow)* 81, 941–950.
- Su, H., Xu, T., Ganapathy, S., Shadfan, M., Long, M., Huang, T.H., Thompson, I., Yuan, Z.M., 2014. Elevated snoRNA biogenesis is essential in breast cancer. *Oncogene* 33, 1348–1358.
- Tessarz, P., Santos-Rosa, H., Robson, S.C., Sylvestersen, K.B., Nelson, C.J., Nielsen, M.L., Kouzarides, T., 2014. Glutamine methylation in histone H2A is an RNA-polymerase-I-dedicated modification. *Nature* 505, 564–568.
- Waga, S., Hannon, G.J., Beach, D., Stillman, B., 1994. The p21 inhibitor of cyclin-dependent kinases controls DNA replication by interaction with PCNA. *Nature* 369, 574–578.
- Watanabe-Susaki, K., Takada, H., Enomoto, K., Miwata, K., Ishimine, H., Intoh, A., Ohtaka, M., Nakanishi, M., Sugino, H., Asashima, M., Kurisaki, A., 2014. Biosynthesis of ribosomal RNA in nucleoli regulates pluripotency and differentiation ability of pluripotent stem cells. *Stem Cells* 32, 3099–3111.
- Xu, X., Xiong, X., Sun, Y., 2016. The role of ribosomal proteins in the regulation of cell proliferation, tumorigenesis, and genomic integrity. *Sci. China Life Sci.* 59, 656–672.
- Yelick, P.C., Trainor, P.A., 2015. Ribosomopathies: global process, tissue specific defects. *Rare Dis.* 3, e1025185.
- Zink, D., 2006. The temporal program of DNA replication: new insights into old questions. *Chromosoma* 115, 273–287.